Title
An extended trajectory-mechanics approach for calculating two-phase flow paths

Journal
AIP Advances, 10(9)

ISSN
2158-3226

Author
Vasco, DW

Publication Date
2020-09-01

DOI
10.1063/5.0017504

Peer reviewed

AIP Advances

An extended trajectory-mechanics approach for calculating two-phase flow paths

Cite as: AIP Advances **10**, 095205 (2020); https://doi.org/10.1063/5.0017504
Submitted: 08 June 2020 . Accepted: 06 August 2020 . Published Online: 01 September 2020

D. W. Vasco

An extended trajectory-mechanics approach for calculating two-phase flow paths

Cite as: AIP Advances 10, 095205 (2020); doi: 10.1063/5.0017504
Submitted: 8 June 2020 • Accepted: 6 August 2020 •
Published Online: 1 September 2020

D. W. Vasco[a]

AFFILIATIONS

Energy Geosciences Division, Building 74, Lawrence Berkeley National Laboratory, 1 Cyclotron Road, Berkeley, California 94720, USA

[a]Author to whom correspondence should be addressed: dwvasco@lbl.gov

ABSTRACT

A technique originating in quantum dynamics is used to derive a trajectory-based, semi-analytical solution for two-phase flow. The partial differential equation governing the evolution of the aqueous phase is equivalent to a family of ordinary differential equations defined along a path through the porous medium. The trajectories may be found by solving the differential equations directly or by post-processing the output of a numerical solution to the full set of governing equations. The trajectories, which differ from conventional streamlines, are found to bend downward in response to gravitational forces. The curvature is more pronounced as the dip of the porous layer containing the flow increases. Subtle changes in the relative permeability curve can lead to significant variations in the trajectories. The ordinary differential equation for the trajectory provides an expression for the travel time along the path. The expression produces a semi-analytical approximation to the model parameter sensitivities, the partial derivatives of the travel times with respect to changes in the permeability model. The semi-analytical trajectory-based sensitivities generally agree with those computed using a numerical reservoir simulator and a perturbation approach. The sensitivities are useful in tomographic imaging algorithms designed to estimate the spatial variation in permeability within a porous medium using multiphase observations.

I. INTRODUCTION

Multiphase fluid flow in a porous medium is a coupled nonlinear process with important applications in energy extraction and environmental remediation.[1,2] Outside of the laboratory, in natural settings, porous media hosting fluid flow are typically very heterogeneous, with permeabilities that can vary by several orders of magnitude. Due to this complexity, the equations describing fluid flow are almost always solved numerically.[2,3] Well formulated numerical approaches provide rigorous solutions but limited insight. Analytic solutions can reveal controlling factors and physical dependencies but are typically restricted to specialized situations, such as a homogeneous whole space or horizontal layers, or by neglecting effects such as capillarity.[4] There is a need for semi-analytical solutions that are generally valid yet still reveal the physics of multiphase flow. Trajectory-based asymptotic approaches can provide more broadly applicable semi-analytical solutions, but they are still only valid under some limiting condition, such as smoothly varying heterogeneity or in the limit of high frequency.[5,6] However, an alternative trajectory-based approach, the one that does not rely on an asymptotic approximation, arose in quantum mechanics through the work of Bohm.[7,8] More recently, this approach has been used to model the quantum mechanical behavior of larger chemical systems and diffusive behavior.[9–14] Here, I use the technique to develop a trajectory-based semi-analytical solution for multiphase flow that is valid under fairly general conditions. These results extend the tracer transport solution of Vasco *et al.*[15] to the much more complicated case of multiphase flow.

II. METHODOLOGY

A. Governing equation

The equations governing the flow of two or more fluids in a porous medium have appeared in many publications. A particularly clear derivation is presented in the work of Peaceman,[3] for example. Consider flow in a porous medium containing two fluids, an

aqueous phase and a non-aqueous phase. In that case, the coupled equations for fluid saturations and fluid pressures may be reduced to a single equation for the saturation of one of the fluid phases and an equation for the average pressure in the two fluids. The governing equation for the saturation of the aqueous phase is considered here. The saturation of the aqueous phase is denoted by S_w, while that of the non-aqueous phase is given by S_n. In general, quantities associated with the aqueous phase are denoted by a subscript w, while the non-aqueous phase quantities are denoted by a subscript n. Because the saturations sum to unity, one may write S_n in terms of the saturation of the aqueous phase,

$$S_n = 1 - S_w.$$

As the compressibility of water is small, it will be assumed that the density of the aqueous phase is constant within the porous medium under consideration. In this case, the governing equation for the saturation, S_w, is given by[6]

$$\varphi \frac{S_w}{\partial t} + \nabla \cdot f_w[\mathbf{q} + \lambda_n(\rho_w - \rho_n)g\mathbf{z}] - \nabla \cdot h_w \nabla S_w = \frac{Q_w}{\rho_w}, \quad (1)$$

where φ is the porosity of the medium, $\mathbf{q}$ is the total velocity of the fluid, ρ_w is the density of the aqueous phase, ρ_n is the density of the non-aqueous phase, λ_n is the phase mobility of the non-aqueous phase, given by

$$\lambda_n = \frac{k_{rn}(S_w)k}{\mu_n}, \quad (2)$$

where $k_{rn}(S_w)$ is the relative permeability function for the non-aqueous phase, k is the absolute permeability, and μ_n is the viscosity of the non-aqueous phase; a similar expression holds for the aqueous phase. The term Q_w on the right-hand-side is the flow rate with units of mass per unit volume per unit time. Because both sides of Eq. (1) have been divided by ρ_w, the units of each term are $[T]^{-1}$. The relative permeability functions, plotted in Fig. 1, quantify the ability of one fluid phase to block the flow of the other. The relative permeabilities are unit-less fractions, where 0 indicates no flow at that saturation and 1 indicates the unimpeded flow. The function $f_w(S_w)$ is the fractional flow curve, given by

$$f_w(S_w) = \frac{\lambda_w}{\lambda_w + \lambda_n}, \quad (3)$$

which is the ratio of the water mobility to the total mobility of the fluid mixture within the pore space. The quantity λ_w is the phase mobility of water, analogous to that for the non-aqueous phase given in Eq. (2). Each fluid has a distinct pressure, and the difference in the two fluid pressures is known at the capillary pressure, $P_c = P_n - P_w$. The capillary pressure is often assumed to be a function of the saturation of one of the phases. The specification of the capillary pressure as a function of the saturation of water is an important property of the medium, and it is typically determined from fitting a functional form to laboratory observations. In Fig. 2, we plot the capillary pressure curve and its derivative with respect to the saturation of a model of a porous medium published by van Genuchten.[16] The coefficient $h_w(S_w)$ in Eq. (1) accounts for the influence of capillary pressure and takes the following form:

$$h_w(S_w) = -f_w \lambda_n \frac{dP_c}{dS_w}. \quad (4)$$

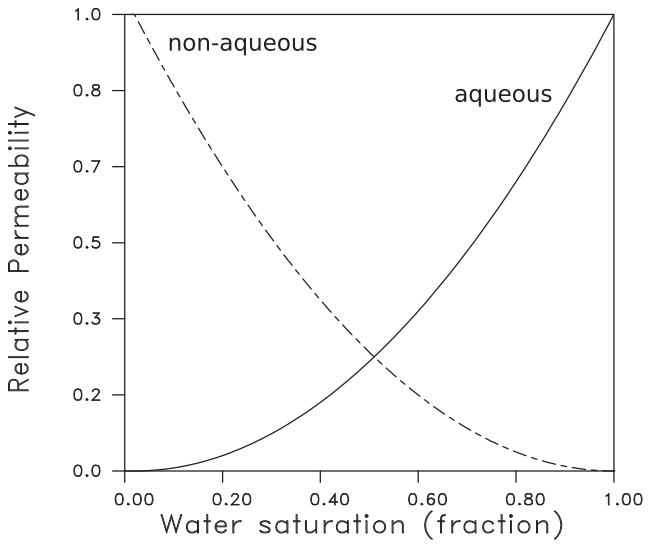

FIG. 1. Relative permeability functions, $k_{rw}(S_w)$ and $k_{rn}(S_w)$, for the flow of an aqueous phase and a non-aqueous phase in a porous medium. The relative permeability model of Stone[17] for three fluid phases is used for these calculations. The third phase has been set to zero.

If I define

$$g_w = f_w \lambda_n (\rho_w - \rho_n) g, \quad (5)$$

where g is the gravitational attraction, and

$$Q_v = \frac{Q_w}{\rho_w}, \quad (6)$$

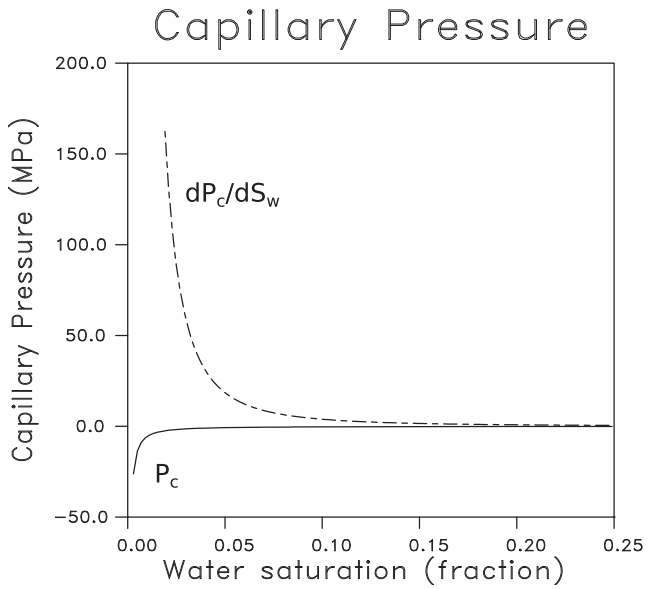

FIG. 2. Capillary pressure curve of van Genuchten[16] and its derivative for the porous medium under consideration. The derivative curve has been cut off in order to retain a vertical scale that displays the variation in capillary pressure, $P_c(S_w)$.

then Eq. (1) may be written as

$$\varphi \frac{S_w}{\partial t} + \nabla \cdot [f_w \mathbf{q} + g_w \mathbf{z}] - \nabla \cdot h_w \nabla S_w = Q_v. \tag{7}$$

The three functions $f_w(S_w)$, $g_w(S_w)$, and $h_w(S_w)$ constitute important elements of the equation-of-state for the flow of water in a porous medium containing a non-aqueous phase. These functions are plotted in Fig. 3 for a model that corresponds to the relative permeability and capillary pressure curves in Figs. 1 and 2. Note from Eq. (4) that if the capillary pressure vanishes or is independent of the water saturation, then h_w vanishes. Expanding the derivatives in Eq. (7), and noting that the functions f_w, g_w, and h_w depend upon both the spatial coordinates $\mathbf{x}$ and the saturation, one can write Eq. (7) as

$$\varphi \frac{S_w}{\partial t} + \boldsymbol{\Upsilon} \cdot \nabla S_w + \frac{dh_w}{dS_w} \nabla S_w \cdot \nabla S_w + h_w \nabla \cdot \nabla S_w = \hat{Q}, \tag{8}$$

where the vector $\boldsymbol{\Upsilon}$ is described below. The right-hand-side $\hat{Q}$ is given by

$$\hat{Q} = Q_v - \nabla_x f_w \cdot \mathbf{q} - f_w \nabla \cdot \mathbf{q} - \nabla_x g_w \cdot \mathbf{z}, \tag{9}$$

with ∇_x signifying that the gradient is with respect to the spatial variables only and S_w is held fixed. Such a gradient with respect to spatial variables $\mathbf{x}$ will vanish if the parameters of the function $h_w(\mathbf{x}, S_w)$ are constant in a region of interest. For example, in our illustrations below, we consider flow in a layer with constant properties, and hence, $\nabla_x h_w$ vanishes. Equation (8) is a non-linear partial differential equation for the saturation with coefficients that depend upon S_w as well as spatial variables $\mathbf{x}$.

The vector $\boldsymbol{\Upsilon}$ is related to the velocity of the water saturation and depends upon the equation-of-state functions and their derivatives,

$$\boldsymbol{\Upsilon} = \frac{df_w}{dS_w} \mathbf{q} + \frac{dg_w}{dS_w} \mathbf{z} + \nabla_x h_w. \tag{10}$$

Note that the vector $\boldsymbol{\Upsilon}$ contains contributions from the flow field, the gravitational field, and capillary forces. The coefficients of the vector terms $\mathbf{q}$ and $\mathbf{z}$, corresponding to the model of Stone[17] are plotted in Fig. 3 along with $h_w(S_w)$. Note how the coefficients grow in magnitude as the aqueous phase approaches full saturation and then vanish very close to $S_w = 1$. For the fractional flow, the faster velocity associated with higher water saturations means that the fluid front will compress or sharpen as the higher saturations overtake the lower saturations. The curve for dg_w/dS_w suggests that the gravitational effect is strongest when the water saturation is large. Furthermore, the force of gravity can either broaden or compress a fluid front, depending on its orientation with respect to the vector $\mathbf{z}$.

B. A trajectory-based solution

It is not possible to find an analytic solution of Eq. (7) unless significant approximations are invoked. Typically, numerical methods, such as finite differences or finite volume methods,[2,18] are employed. In this section, we develop a semi-analytical trajectory-based solution requiring numerical techniques for its construction. The general foundation of the method is an approach used in quantum mechanics to treat the time-dependent Schrödinger equation.[10–12,14] There are some advantages associated with such

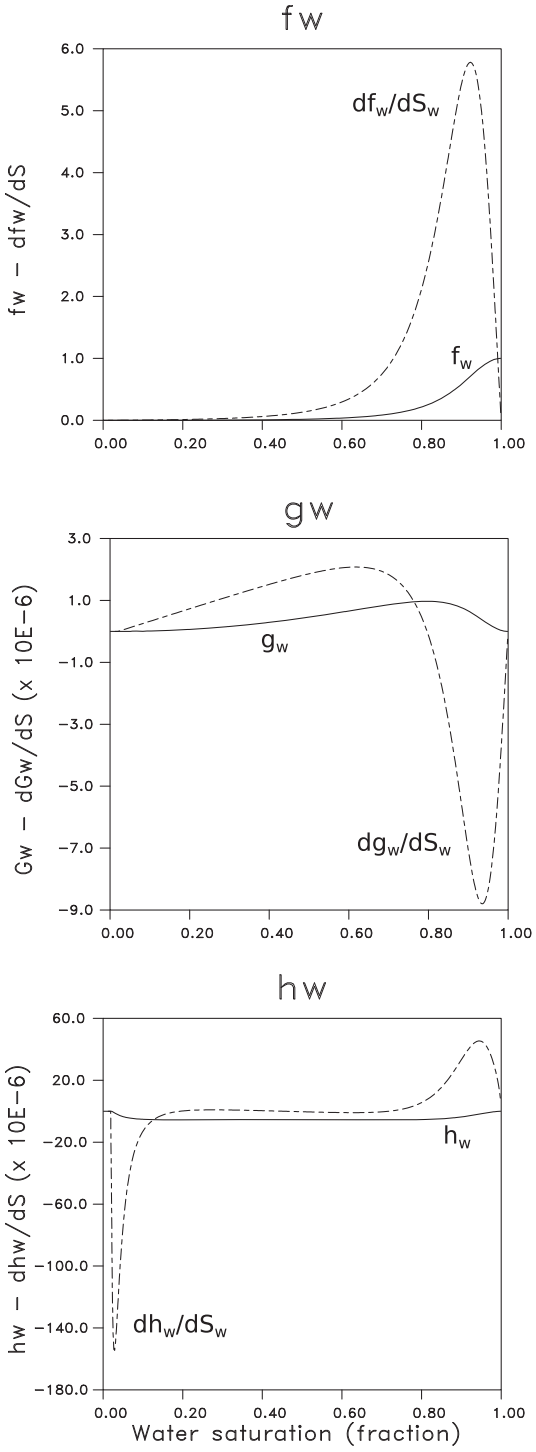

FIG. 3. Equation-of-state functions corresponding to the formulation of *Stone*.[17] The three functions are (upper panel) the fractional flow of water, as given by Eq. (3), (middle panel) the influence of gravity on the flow, g_w, expressed by Eq. (5), and (lower panel) the influence of capillary pressure $h_w(S_w)$ presented in Eq. (4). Both the equation-of-state functions and their derivatives with respect to changes in water saturation S_w are shown.

a solution. For example, it requires less computation than a full numerical treatment and can be used on larger problems.[14] The trajectories provide physical insight and are useful for the visualization of complex fluid transport. In that sense, the solution is similar to streamline modeling techniques[19] though the extended approach is more general and accounts for cross-streamline processes through the coupling of adjacent trajectories.[14]

Following Garashchuk and Vazhappilly,[11] consider an exponential representation of the dependent variable,

$$S_w(\mathbf{x}, t) = e^{-\Omega(\mathbf{x},t)}, \tag{11}$$

in order to derive the equations defining the solution. Because the saturation is a fraction and is unit-less, Eq. (11) is dimensionally correct. The transformation (11) is well defined for a saturation distribution that is always positive. If the saturation vanishes in a region, one can modify Eq. (11) to only hold in areas of non-zero water saturation. Alternatively, a small, non-zero background saturation could be imposed in order to avoid ill-defined situations. The time derivative transforms as

$$\frac{\partial S_w}{\partial t} = -\frac{\partial \Omega}{\partial t} e^{-\Omega} \tag{12}$$

and the spatial gradient transforms as

$$\nabla S_w = -\nabla \Omega e^{-\Omega} \tag{13}$$

and similarly for higher-order spatial derivatives in the term $\nabla \cdot \nabla S_w$. Substituting the representation (11) into the governing equation (8) and transforming the derivatives gives

$$\varphi \frac{\partial \Omega}{\partial t} + (\boldsymbol{\Upsilon} - H_w \nabla \Omega) \cdot \nabla \Omega = \hat{Q} e^{\Omega} - h_w \nabla \cdot \nabla \Omega, \tag{14}$$

where

$$H_w = \frac{dh_w}{dS_w} S_w + h_w = \frac{dh_w}{dS_w} e^{-\Omega} + h_w \tag{15}$$

is a coefficient that vanishes if capillary pressure effects are not important, eliminating a highly non-linear term from Eq. (14). From a plot of this function in Fig. 4, it is clear that the coefficient H_w is most significant where the water saturation is high and the saturation of the non-aqueous phase is low.

For a given flow field $\mathbf{q}$, Eq. (14) is a self-contained non-linear partial differential equation for Ω. This equation serves as an entry point to approximation techniques based upon the assumptions of a smoothly varying medium, similar in spirit to asymptotic methods. Specifically, if it is assumed that the medium has smoothly varying properties, leading to a gradually varying saturation field, then the final curvature term $h_w \nabla \cdot \nabla \Omega$ in Eq. (14) may be neglected. The resulting equation is a non-linear, first-order partial differential equation for Ω, related to a family of Hamilton–Jacobi equations[20] containing the well known eikonal equation as an example. A derivation of a trajectory-based solution based upon this approximation is given in the work of Vasco and Datta-Gupta.[6]

No such approximation will be made here, rather Eq. (14) is treated directly, retaining all of its terms. Our approach is motivated by the work of Garashchuk[10] in her study of propagation of a disturbance with a momentum-dependent potential. For brevity, one can define the slowness vector of the water saturation S_w,

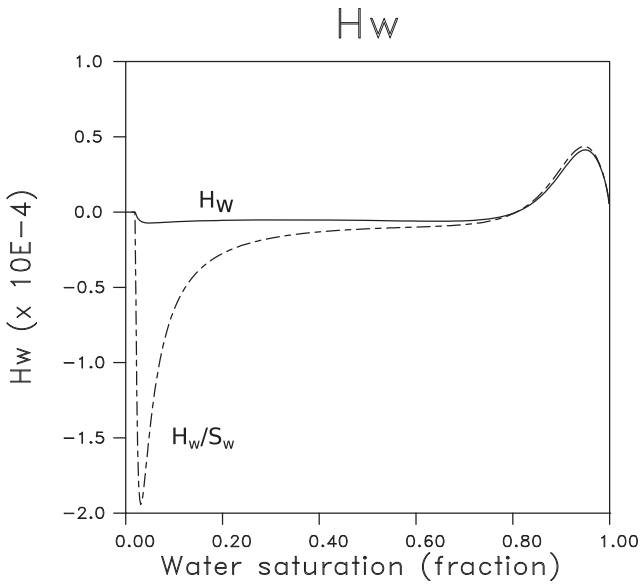

FIG. 4. (Solid line) The capillary pressure sensitivity function $H_w(S_w)$. (Dashed line) The function $H_w(S_w)$ divided by S_w, which controls the sensitivity of the trajectory to the gradient of the saturation field, ∇S_w.

$$\mathbf{p}_w = \nabla \Omega, \tag{16}$$

and the water velocity vector,

$$\mathbf{v}_w = \frac{1}{\varphi}(\boldsymbol{\Upsilon} - H_w \mathbf{p}_w), \tag{17}$$

and write Eq. (14) as

$$\frac{\partial \Omega}{\partial t} + \mathbf{v}_w \cdot \nabla \Omega = \frac{1}{\varphi}\left(\hat{Q} e^{\Omega} - h_w \nabla \cdot \mathbf{p}_w\right). \tag{18}$$

Consider a Lagrangian reference frame that moves along one coordinate axis, described by a trajectory $\mathbf{x}_w(t)$, with the velocity vector $\mathbf{v}_w$. The total time derivative along the trajectory is given by

$$\frac{d\Omega}{dt} = \frac{\partial \Omega}{\partial t} + \mathbf{v}_w \cdot \nabla \Omega = \frac{\partial \Omega}{\partial t} + \frac{d\mathbf{x}_w}{dt} \cdot \nabla \Omega. \tag{19}$$

From the equations given above, it is possible to deduce an equivalent set of ordinary differential equations that may be solved for $\Omega(\mathbf{x}(t), t)$, defined along trajectories or paths $\mathbf{x}(t)$ through the porous medium. The first equation defining the trajectory-based solution, following directly from (19), is given by

$$\frac{d\mathbf{x}_w}{dt} = \mathbf{v}_w = \frac{1}{\varphi}(\boldsymbol{\Upsilon} - H_w \mathbf{p}_w), \tag{20}$$

where we have made use of the definition (17). A second expression is obtained if we use (19) to substitute for the left-hand-side of Eq. (18),

$$\frac{d\Omega}{dt} = \frac{1}{\varphi}\left(\hat{Q} e^{\Omega} - h_w \nabla \cdot \mathbf{p}_w\right). \tag{21}$$

A third and final equation for $\mathbf{p}$ follows by taking the spatial gradient of Eq. (21) and using the definition (16) to write

$$\frac{d\mathbf{p}_w}{dt} = \nabla\left[\frac{1}{\varphi}\left(\hat{Q}e^{\Omega} - h_w \nabla \cdot \mathbf{p}_w\right)\right]. \quad (22)$$

The three equations (20)–(22) are equivalent to the partial differential equation (18) and provide an alternative means for obtaining its solution.

In order to complete the system of equations for modeling the two-phase flow, we need an expression for the total flow velocity **q**. As the trajectory calculations will rely on a numerical simulator to determine critical quantities, as discussed in Subsection II C, this is not a pressing issue because one can extract **q** from the simulation results. However, as in streamline simulation,[19] it is possible to compute the pressure field numerically in conjunction with the saturation estimates. Alternatively, one can formulate a trajectory-based solution of the pressure equation in the case of single-phase flow.[21] This technique may be extended to the flow of two or more fluids, leading to a full set of ordinary differential equations for variations in both saturation and fluid pressure.

Given a flow field, **q**, Eqs. (20)–(22) form a system of ordinary differential equations that may be solved using numerical methods.[23,24] That is, given the appropriate initial and/or boundary conditions, one may integrate the equations numerically to determine the trajectory $\mathbf{x}_w(t)$, the vector $\mathbf{p}_w(t)$, and $\Omega(t)$. As noted by Wyatt,[14] the presence of the spatial gradients in Eqs. (21) and (22) introduces off-trajectory components of $\mathbf{p}_w$ and the medium properties adjacent to the trajectory into the calculation of a trajectory. Therefore, the trajectory computations are coupled and one must introduce more sophisticated numerical methods, such as the calculation of families of trajectories, in order to solve the system.[14]

C. Calculating trajectories with the help of a numerical simulator

As noted above, the conventional method for solving the equations governing two-phase flow is by numerical methods that include finite-volume, finite-difference, and finite-element techniques. Thus, a number of such routines are readily available and may be used to compute the evolution of $S_w(\mathbf{x}, t)$ for a given set of initial and boundary conditions. For example, the numerical simulator TOUGH2[18] was used to calculate the pressure and saturation changes due to the injection of water into an air saturated porous layer that dips 30° to the south. The layer permeability (k) is 2.0 $\times 10^{-13}$ m^2, and the porosity (φ) is 0.10. The grid blocks adjacent to the boundary are given extremely large volumes so that their pressure does not change significantly from its initial value, effectively creating a constant pressure boundary condition. The out-of-plane top and bottom boundaries of the layer are subject to no-flow conditions, restricting flow to within the layer. The lateral boundaries are also 1000 m away from the edges of the grid blocks plotted in Fig. 5 so that the effects of these boundary condition are not visible in this figure. Water is injected into the air filled layer at a rate of 300.0 kg/s. The results of the simulation after 464 days are plotted in Fig. 5.

If one is interested in obtaining the trajectories $\mathbf{x}_w(t)$ for visualizing the movement of the fluid phases, or for use in the inverse problem,[6] then it is possible to take advantage of the existing numerical simulators for the path calculations. Specifically, solving Eq. (11) for $\Omega(\mathbf{x}, t)$ gives

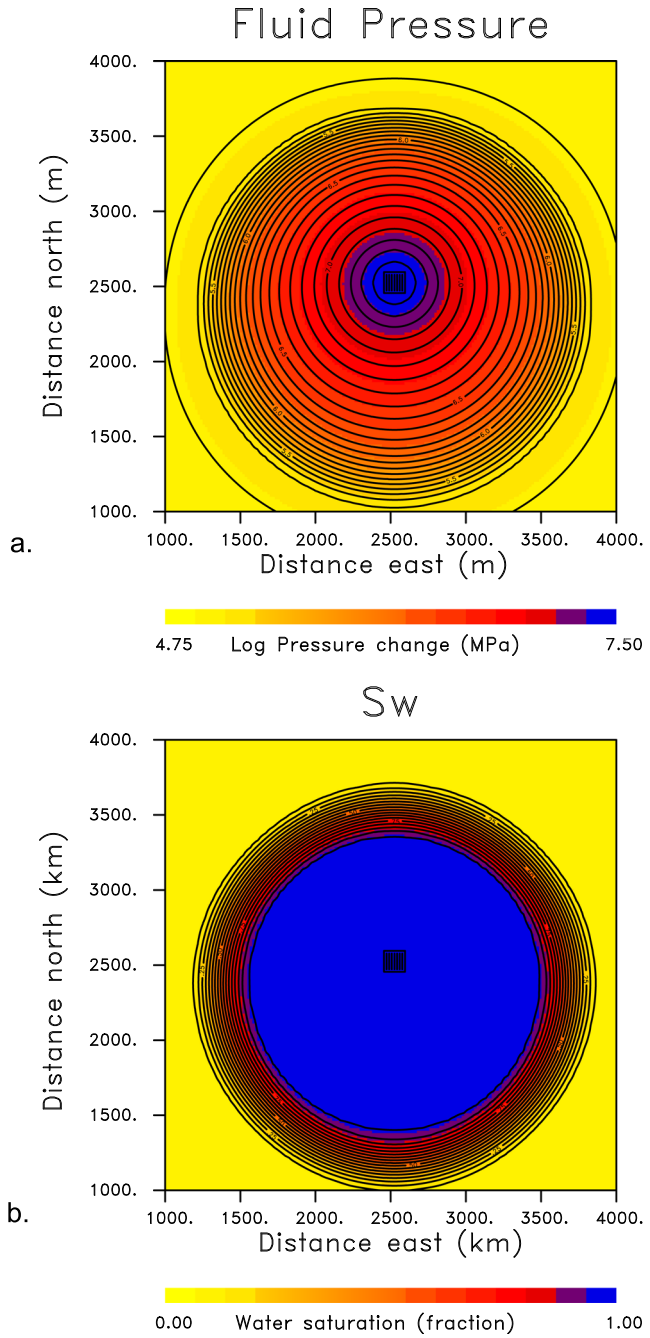

FIG. 5. (a) Average fluid pressure change and (b) water saturation after 464 days of injection in the central well denoted by the filled square. Water is injected in an air-filled layer that dips 30° to the south.

$$\Omega(\mathbf{x}, t) = -\ln S_w(\mathbf{x}, t). \quad (23)$$

Combining this with Eq. (16) provides an expression for $\mathbf{p}_w$ that may be substituted into Eq. (20) to give

$\frac{df_w}{dS_w}\mathbf{q}$

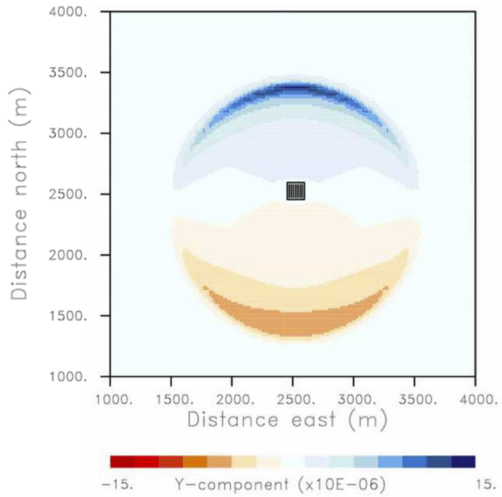

$\frac{dg_w}{dS_w}\mathbf{z}$

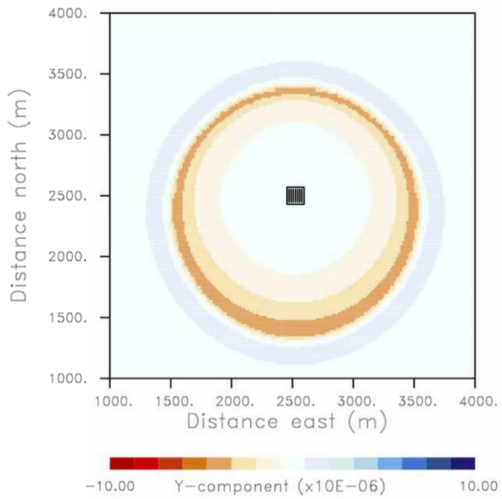

$H_w/S_w\nabla S_w$

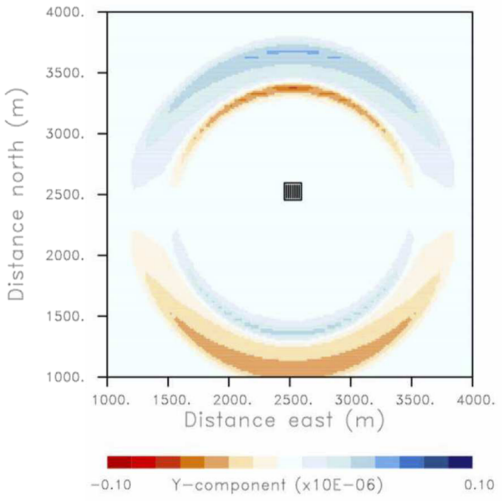

FIG. 6. Three primary contributions to the y-component of the velocity vector, corresponding to the state of the layer after 464 days of injection. (Top panel) The contribution of the y-component flow field vector **q** to the velocity vector $\mathbf{v}_w$. (Central panel) The contribution to the y-component of $\mathbf{v}_w$ due to the gravitational force in the direction of the vector **z**. (Bottom panel) The contribution to the y-component of the velocity vector due to the gradient of the saturation field, ∇S_w.

$$\frac{d\mathbf{x}_w}{dt} = \frac{1}{\varphi}(\boldsymbol{\Upsilon} + H_w \nabla \ln S_w) \tag{24}$$

or

$$\frac{d\mathbf{x}_w}{dt} = \frac{1}{\varphi}\left[\boldsymbol{\Upsilon} + \left(\frac{dh_w}{dS_w} + \frac{1}{S_w}h_w\right)\nabla S_w\right], \tag{25}$$

an ordinary differential equation for the trajectory that may be integrated directly. Note from Fig. 1 that for low water saturation, S_w, of less than 5%, the fractional flow function $f_w(S_w)$ and, hence, $h_w(S_w)$ defined by Eq. (4) are zero. The quantity in parentheses in Eq. (25) is H_w/S_w and is plotted as the dashed line in Fig. 4. It is most significant for both low and high water saturations, that is, for saturations less than 0.3 and for those greater than 0.8. From the equation for the trajectory (25) and the form of the vector $\boldsymbol{\Upsilon}$, it is evident that the trajectory depends upon the flow field $\mathbf{q}$, the gravitational force vector directed along $\mathbf{z}$, and the gradient of the saturation field ∇S_w. Furthermore, if there are spatial variations in the capillary pressure dependence, there will be an additional $\nabla_x h_w$ term in $\boldsymbol{\Upsilon}$.

From the TOUGH2 simulation results in Fig. 5, one observes that the velocity field $\mathbf{q}$ is roughly parallel to the vector field due to the saturation gradient ∇S_w. The component of the gravitational vector $\mathbf{z}$ within the dipping layer is a uniform vector field directed toward the southern edge of the layer. Because the capillary properties of the layer are constant, the spatial gradient term $\nabla_x h_w$ in $\boldsymbol{\Upsilon}$ vanishes. Thus, there are three main contributions to the right-hand-side of Eq. (25): a term describing the contribution of the flow field, a term describing the contribution of the gravitational force, and a term representing capillary effects that described the sensitivity to the existing saturation distribution, in particular to the gradient of the water saturation. The y-component of each of the three contributions to the velocity vector $\mathbf{v}_w$ is plotted in Fig. 6. I focus on the y-component because that is the direction along which the gravitational force acts; hence, it displays all of the major contributions to the velocity vector $\mathbf{v}_w$. The vector contributions are for a snapshot at 464 days, corresponding to the saturations and pressures shown in Fig. 5. Note that the dominant contribution is associated with the flow field $\mathbf{q}$ and it provides motion away from the injection point. The vector component associated with the gravitational force is the second largest contribution, and it is in the downward or southern (negative) direction due to the dip of the layer. The capillary force associated with $H_w(S_w)$ is the smallest contribution, roughly two orders of magnitude smaller than that of the flow field. As with the contribution due to the flow field, the movement is outward from the source at the outer margin of the saturation front shown in Fig. 5, but there is a component in the reverse direction on the inward side of the saturation front, suggesting that the capillary force is spreading the front.

As indicated in Eq. (25), the velocity vector $\mathbf{v}_w$ associated with the water flowing from the injection point is the sum of the three contributions that are plotted in Fig. 6. Given the flow field, we can integrate the three equations (20)–(22) to obtain the trajectories. Alternatively, given the results from a numerical simulation of the two-phase flow, we can use the simulation history to integrate Eq. (25) for the path $\mathbf{x}_w(t)$. In Fig. 7, we plot twelve trajectories describing the flow from the injection well to the edge of the model. As indicated by the contributions plotted in Fig. 6, the flow is primarily outward from the injection point, with a downward

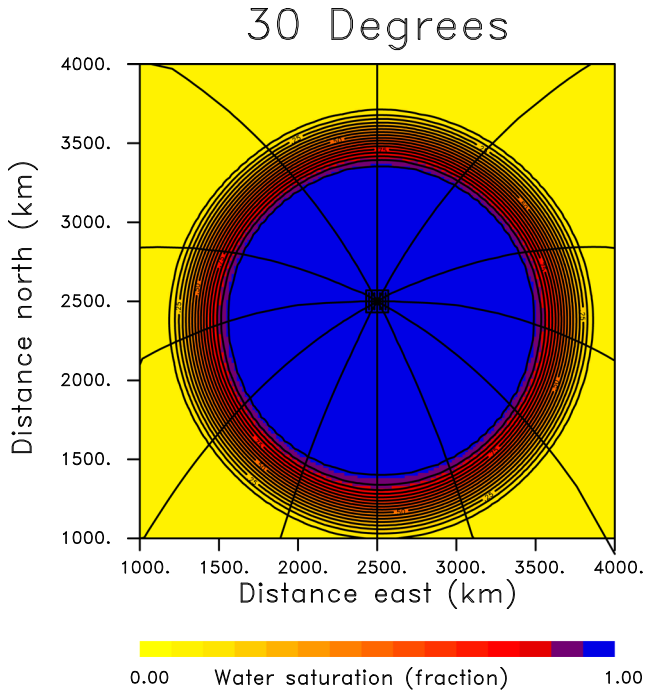

FIG. 7. Trajectories associated with fluid flow due to injection into a porous layer that is dipping 30° to the south. The paths are obtained by integrating the differential equation (25) from the injection point to the edge of the model.

contribution from the gravitational force. Note that the trajectories are not normal to the saturation front, or to the pressure contours shown in Fig. 5, due to the influence of gravity on the fluid flow. That is, from the relative sizes of the contributions to the vector field plotted in Fig. 6, one observes that the flow ($\mathbf{q}$) and gravity ($\mathbf{z}$) components are of the same order, while the component due to capillary effects (∇S_w) is two orders of magnitude smaller.

III. ILLUSTRATIONS AND APPLICATIONS

In this section, I calculate the extended trajectories and illustrate their variation due to differences in the dip of a layer, leading to changes in the gravitational force. In addition, there is an example documenting how variations in the relative permeability functions can change the trajectories. Finally, the approach is applied to the calculation of model parameter sensitivities. In this case, I consider the sensitivity of the arrival time of the saturation front to perturbations in the permeability at points along the trajectory.

A. The influence of gravity

Gravitational forces, coupled with density variations between the fluids and density changes due to a time-varying pressure field, can lead to complicated flow in a porous medium. While it is possible to model the flow using the differential equations (20)–(22), in conjunction with an equation for the time-varying pressure field, for this illustration, the TOUGH2 numerical simulator is used to

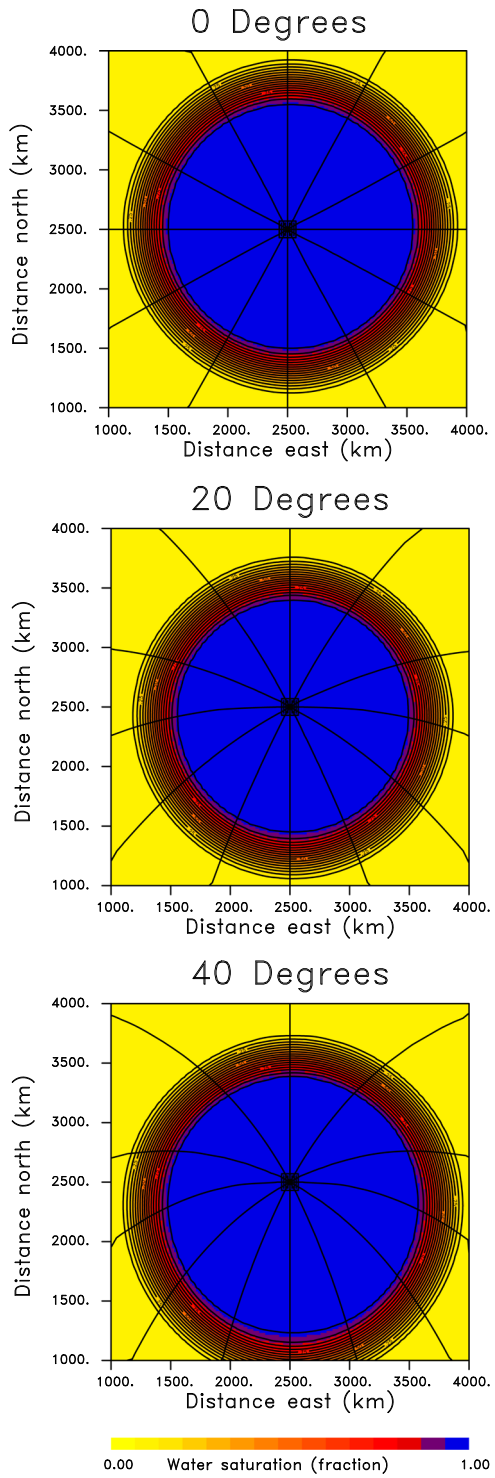

FIG. 8. The color scale indicates the saturation distribution after 464 days in each panel, for layers of varying dip in the north-source (y) direction. The trajectories indicate the flow paths resulting from the competing effects of the flow field **q**, the force of gravity in the **z** directions, and the capillary forces, which are in the direction ∇S_w in this homogeneous layer.

solve the governing equations. The resulting saturation and pressure fields are post-processed in order to calculate the trajectories using Eq. (25). The gravitational force is varied by changing the dip of the layer. Initially, the layer is horizontal, that is, the dip to the south is 0.0° leading to radial trajectories extending from the injection well to the outer edges of the model (Fig. 8). As the dip increases to 20° and then 40°, the trajectories increasingly bend to the south in response to the increased influence of gravity on the flow.

B. An alternative relative permeability model

Given the direct dependence of the functions $f_w(S_w)$, $g_w(S_w)$, and $h_w(S_w)$ on the fractional flow of water, it appears that the trajectories will depend strongly on the relative permeabilities of the aqueous and non-aqueous phases. The preceding results were based upon the relative permeability model of Stone.[17] However, there are a wide array of relative permeability functions and any specification of one of a family of such functions will depend upon laboratory observations calibrated to a particular material.[24] In order to illustrate the variability that arises from the use of a different relative permeability function, we consider one alternative model, which was proposed by Parker *et al.*[25] These particular relative permeability curves are plotted in Fig. 9. Although the relative permeability curves of Stone[17] and Parker *et al.*[25] are generally similar, they differ in a few details. The most significant difference is the decrease in the aqueous relative permeability to values near zero at a saturation S_w of around 30%. Thus, the fluid is not mobile until a relatively high fraction of the pore space is occupied by the aqueous phase. Even small features, such as the fact that non-aqueous phase relative permeability goes to zero just before a value of S_w that is less than 1 in the Stone[17] model,

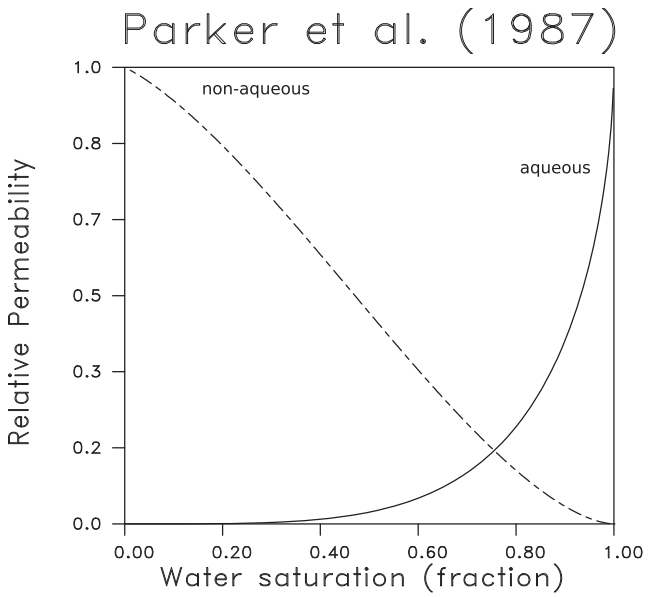

FIG. 9. Relative permeability functions proposed by Parker *et al.*,[25] based upon the capillary pressure function of van Genuchten.[16]

while it does not in the Parker *et al.*[25] model, can lead to differences in the trajectories.

For comparison, consider the homogeneous layer dipping at 30° to the south, which was discussed above, with the same values for porosity, φ, and absolute permeability, k. The north–south asymmetry, visible in the saturation distribution in Fig. 7, is not evident in the results from the Parker *et al.*[25] model (Fig. 10). The roughly symmetric movement of the aqueous fluid is evident in Fig. 10, where the saturation field after 464 days of injection is shown. In addition, the two-phase front plotted in Fig. 10 is broader than the front associated with the Stone[17] model plotted in Fig. 7. The trajectories that result from integrating the defining equation (25) are also plotted in Fig. 10. The paths are nearly radial despite that the layer dips 30° to the south. This contrasts with the results corresponding to the Stone[17] model, as shown in Fig. 7, where the trajectories bend to the south in response due to gravitational forces. Thus, it appears that subtle differences in the relative permeability curves may lead to significant deviations in the trajectories, most likely due to the nonlinearity of the governing equations.

C. Sensitivity computations

Now, consider an application of the methodology to the calculation of model parameter sensitivities. Sensitivities are often used in iterative approaches for solving the inverse problem and for estimating flow properties in a porous medium.[6] Sensitivities are the coefficients in a linearized relationship between a perturbation in a model parameter, such as a grid block permeability in a model of a porous medium, and the resulting deviation in an observed quantity. Here, I consider the arrival time of a jump in the saturation at a given observation point as the basic datum. One can use the trajectories, and expression (25) for the velocity of the saturation along the trajectory, to calculate semi-analytical approximations for the sensitivities. In order to see this, consider the equation written out in full, for the case in which h_w does not vary with $\mathbf{x}$, so that $\nabla_x h_w$ vanishes,

$$\frac{d\mathbf{x}_w}{dt} = \frac{1}{\varphi}\left[\frac{df_w}{dS_w}\mathbf{q} + \frac{dg_w}{dS_w}\mathbf{z} + \left(\frac{dh_w}{dS_w} + \frac{1}{S_w}h_w\right)\nabla S_w\right]. \tag{26}$$

Making use of Darcy's law[1] for a medium containing two phases, one can write the total flow velocity vector $\mathbf{q}$ as

$$\mathbf{q} = \mathbf{q}_w + \mathbf{q}_n = k\left(\frac{k_{rw}}{\mu_w}\nabla P_w + \frac{k_{rn}}{\mu_n}\nabla P_n\right), \tag{27}$$

where $\mathbf{q}_w$ and $\mathbf{q}_n$ are the velocities of the aqueous and non-aqueous phases, respectively. The quantity in brackets contains contributions from $P_w(\mathbf{x}, t)$, the fluid pressure associated with the aqueous phase, and the fluid pressure in the non-aqueous phase weighted by the phase mobilities. Alternatively, one can write the total flow velocity vector in terms of the weighted contributions of the pressure gradients, which is designated as $\mathbf{w}$,

$$\mathbf{q} = k\mathbf{w} = k\left(\frac{k_{rw}}{\mu_w}\nabla P_w + \frac{k_{rn}}{\mu_n}\nabla P_n\right). \tag{28}$$

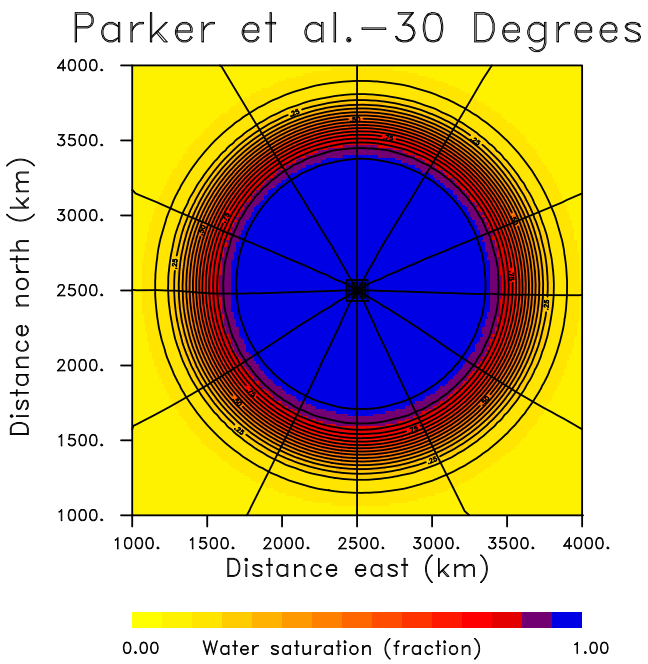

FIG. 10. Results associated with two-phase fluid flow governed by the relative permeability curves of Parker *et al.*[25] The solid lines denote trajectories corresponding to the movement of water away from an injection point denoted by the filled square. The color scale indicated the water saturation within the porous layer after 464 days of injection.

As an illustration, and a means to compare the trajectory-based sensitivities to those obtained by conventional numerical differencing, we can consider a well configuration that is sometimes used in industrial applications. The five-spot, a pattern containing a central well surrounded by four corner wells, is used for both enhanced oil recovery and environmental remediation. The central well may undergo fluid injection or production, depending on the application, while the corner wells are subject to the opposite operation. This pattern is scalable in that one can add wells to make groups of five-spots. No flow boundary conditions can best represent the situation at the edges of a five-spot that lies within such a group. The quarter five-spot, plotted in Fig. 11, represents the corner of the pattern with an injector at the lower-right and a producing well at the upper-left. The steady-state pressure field associated with the injection and production is also plotted in this figure. The porous medium used in this simulation consists of a single, horizontal, homogeneous layer with a porosity of 1% and a permeability of 105 mD. The well at the lower-right corner injects water into a layer containing 65% water and 35% oil. In this example, we will assume that capillary effects are not significant and that we can consider the pressure in the aqueous and non-aqueous phases to be equal.

In order to determine the trajectory, we must integrate the defining equation (26), an ordinary differential equation for the path. Because every term in the equation contains the absolute permeability, k, we can factor it out to write the differential equation as

$$\frac{d\mathbf{x}_w}{dt} = \mathbf{v}_w = \frac{k}{\varphi}\left[W\mathbf{w} + H\nabla S_w + G\mathbf{z}\right]. \tag{29}$$

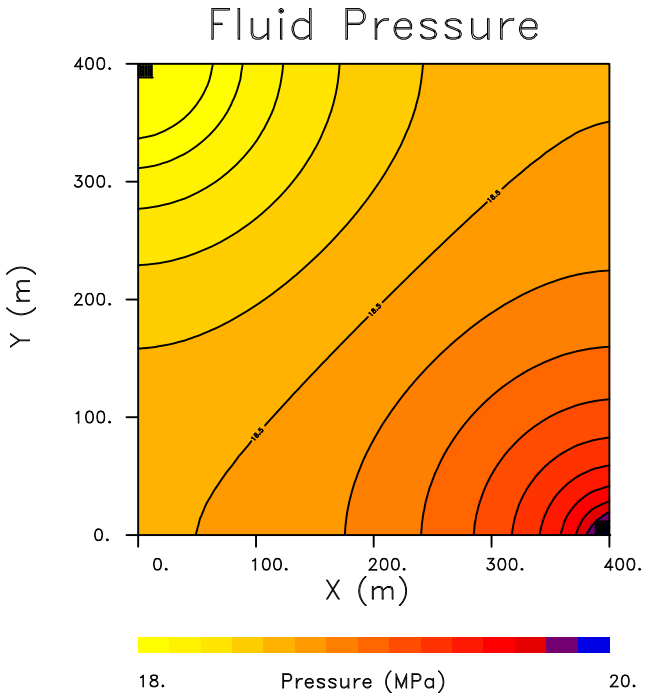

FIG. 11. A quarter five-spot well configuration, consisting of two corner wells, indicated by the black filled squares, with no flow boundary conditions at the edges of the rectangle defined by the wells. The color scale indicates the steady-state pressure field between the two wells.

Even though the explicit dependence upon k has been factored out, both $\mathbf{w}(\mathbf{x}, t)$ and $S_w(\mathbf{x}, t)$ still have an implicit dependence upon $k(\mathbf{x})$. The coefficients are given by

$$W(\mathbf{x}, t; S_w) = \frac{df_w}{dS_w}, \tag{30}$$

$$H(\mathbf{x}, t; S_w) = \frac{d\hat{h}_w}{dS_w} + \frac{1}{S_w}\hat{h}_w, \tag{31}$$

where $\hat{h_w}(\mathbf{x}, S_w)$ is given by $h_w(S_w)$ with $k(\mathbf{x})$ factored out,

$$\hat{h}_w(S_w) = -f_w \frac{k_{rn}}{\mu_n}\frac{dP_c}{dS_w}, \tag{32}$$

see Eqs. (2) and (4), and finally,

$$G(\mathbf{x}, t; S_w) = f_w \frac{k_{rn}}{\mu_n}(\rho_w - \rho_n)g. \tag{33}$$

In our example problem, both the capillary and gravitational forces can be neglected and the vector field defined by Eq. (29) is determined by the pressure field, plotted in Fig. 11, and the fractional flow properties of the medium. Because we are assuming a steady-state flow field, the pressure field is time invariant because there are no density or capillary effects. We can integrate Eq. (29) by starting at the injection well and marching down the pressure gradient to the producing well. The trajectories are distinguished by their take-off angle as they leave the location of the injection well. Thus, we can integrate Eq. (29) using a numerical shooting method[23] or, in this case, using streamline methods.[19] In Fig. 12, we plot the paths connecting the injector and producer for 20 different take-off angles. As in the previous case, the trajectories are not normal to the saturation fronts.

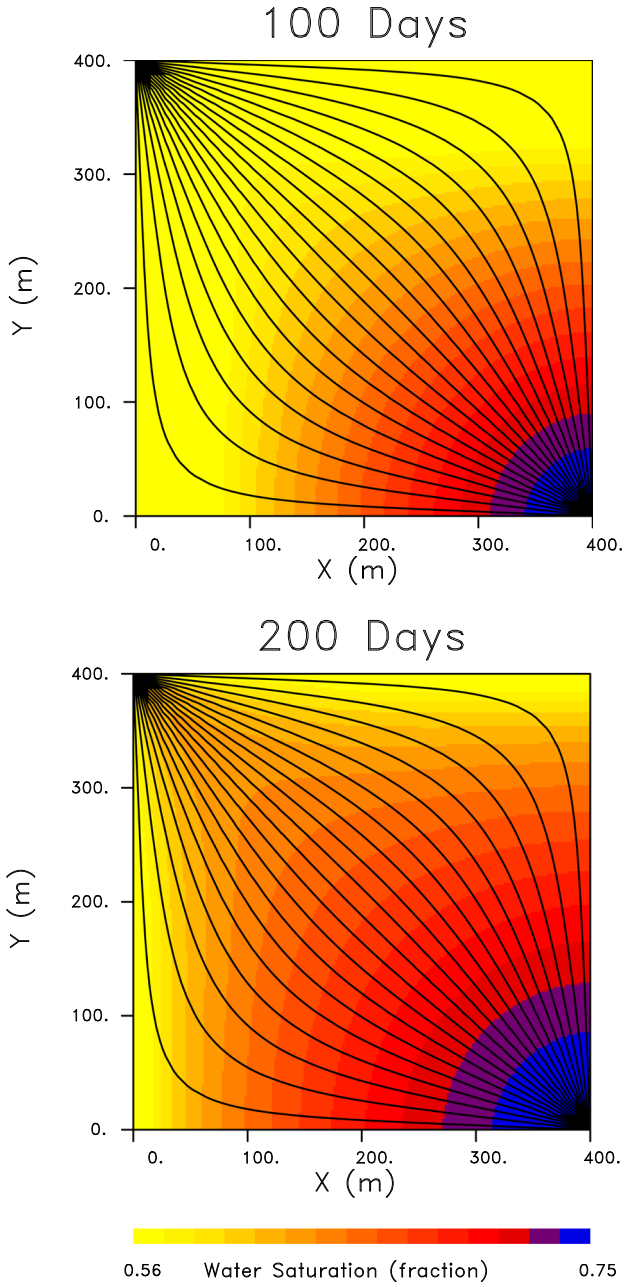

FIG. 12. (Top panel) Saturation distributions after 100 days of injection from the well in the lower-right corner of the quarter five-spot well configuration. (Bottom panel) Saturation distribution after 200 days of injection. The color scale indicates the fractional water saturation within the pore space of the porous layer. The black solid lines are the trajectories obtained by integrating the differential equation (29).

In order to produce an expression for the travel time along the trajectory, one can integrate along the path $\mathbf{x}(s)$, where s signifies the distance or position along the curve. The variable s may represent arc-length or travel time, but it can be left as a general parameter for now. Because $\mathbf{v}_w$ is the tangent vector to the path $\mathbf{x}_w(s)$, the integral for the travel time from the injection point to the point at location s on the trajectory, $T(s)$, is given by

$$T(s) = \int_{\mathbf{x}_w} \frac{dr}{|\mathbf{v}_w|}, \tag{34}$$

where r is the distance along the trajectory. In Fig. 13, the travel times are plotted for the component of S_w that is just above the background water saturation in the porous medium before water injection. The water travels fastest along the diagonal connecting the wells, which is also the shortest path. Water traveling near the boundaries of the rectangular area approaches stagnation points in the upper-right and lower-left corners of the region that are associated with lower flow velocities resulting in greater travel times. We partition the velocity vector $\mathbf{v}_w$, factoring out the explicit φ and k dependence, which is given by

$$\mathbf{v}_w = \frac{k}{\varphi}\mathbf{u}_w, \tag{35}$$

where $\mathbf{u}_w$ is the vector field determined by the contributing vectors $\mathbf{w}$, ∇S_w, and $\mathbf{z}$, given by Eq. (28),

$$\mathbf{u}_w = W\mathbf{w} + H\nabla S_w + G\mathbf{z}. \tag{36}$$

The integral (34) can now be written as

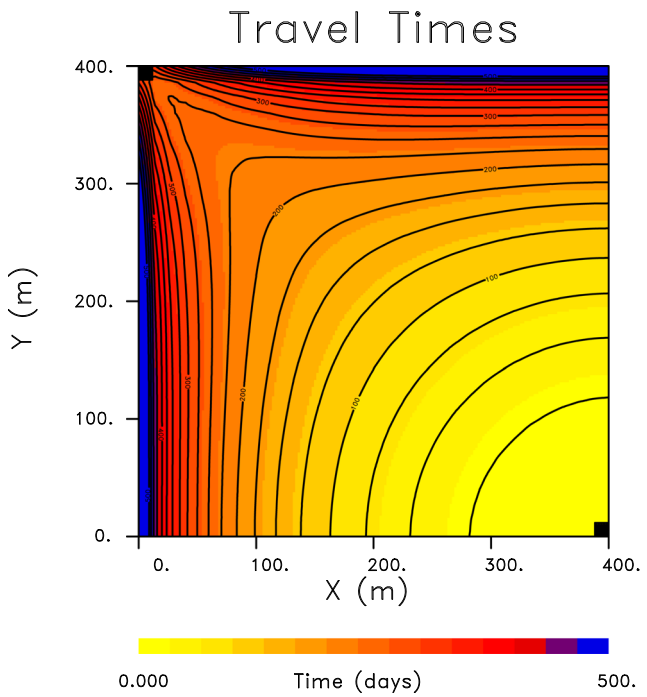

FIG. 13. Travel time field for the saturation component S_w that is 1% higher than the background or the initial water saturation.

$$T(s) = \int_{\mathbf{x}_w} \frac{\varphi}{k}\frac{dr}{|\mathbf{u}_w|}, \tag{37}$$

which contains both an explicit dependence upon k and an implicit dependence through the influence of permeability on the pressure and the saturation.

In order to compute the sensitivity of the arrival time to a perturbation in the permeability, consider an initial or background permeability field $k_o(\mathbf{x})$ and an associated travel time for the saturation to reach a point $\mathbf{x}_r$ upon propagating through the background medium, denoted by $T_o(\mathbf{x}_r)$. If the permeability is perturbed to a new field $k(\mathbf{x}) = k_o(\mathbf{x}) + \delta k(\mathbf{x})$, there will be a corresponding change in the arrival time to $T(\mathbf{x}_r) = T_o(\mathbf{x}_r) + \delta T(\mathbf{x}_r)$. Substituting in for $k(\mathbf{x})$ and $T(\mathbf{x}_r)$ in the integral (38) gives

$$T(s) = T_o(s) + \delta T(s) = \int_{\mathbf{x}_w} \frac{\varphi}{(k_o + \delta k)}\frac{dr}{|\mathbf{u}_w|}. \tag{38}$$

The perturbation will influence both the trajectory itself, $\mathbf{x}_w$, as well as the pressure and saturation fields, and, hence, $\mathbf{u}_w$. However, it has been noted in earlier studies[6,26] that the perturbations in both the path and the saturation and pressure fields appear to be of second order in δT and do not change the sensitivities substantially in comparison with the direct perturbation in $k_o(\mathbf{x})$. For simplicity, I shall assume that such behavior also holds for this more general case. Validation and a more detailed examination will be saved for a later study. Expanding the denominator of (38) in a Taylor series in δk with the retention of first-order terms gives the linearized relationship between a perturbation in permeability and a perturbation in the travel time of the saturation front,

$$\delta T(s) = \int_{\mathbf{x}_o} \frac{1}{k_o}\frac{\delta k}{|\mathbf{u}_o|}dr, \tag{39}$$

where $\mathbf{x}_o$ signifies the trajectory in the background model and $\mathbf{u}_o$ denotes the vector $\mathbf{u}_w$ in the background model. The semi-analytical expression for the model parameter sensitivity for a change in permeability is given by

$$\frac{\partial T}{\partial k} = \frac{1}{k_o}\frac{1}{|\mathbf{u}_o|} \tag{40}$$

and may be computed using a single numerical simulation of the flow in the reservoir for each iterative update of the permeability model. This formulation allows for a tomographic approach for the inversion of two-phase arrival time data. In particular, given an initial or current reservoir model, one reservoir simulation allows for the calculation of all quantities necessary for calculating sensitivities associated with a single experiment or injection from a given source well.

In order to verify that the semi-analytical expression (40) provides a reasonable approximation to the actual permeability sensitivities, we compare it to a purely numerical estimate (Fig. 14). The numerical estimate is obtained using a perturbation approach in which a grid block permeability in a reservoir model is perturbed, and the new travel time of the saturation change to the producing well is calculated using a numerical reservoir simulator. The travel time perturbation is calculated by subtracting the travel time for the unperturbed model. Dividing the travel time perturbation by the permeability deviation in the grid block produces the model parameter sensitivity. This approach requires $N + 1$ reservoir

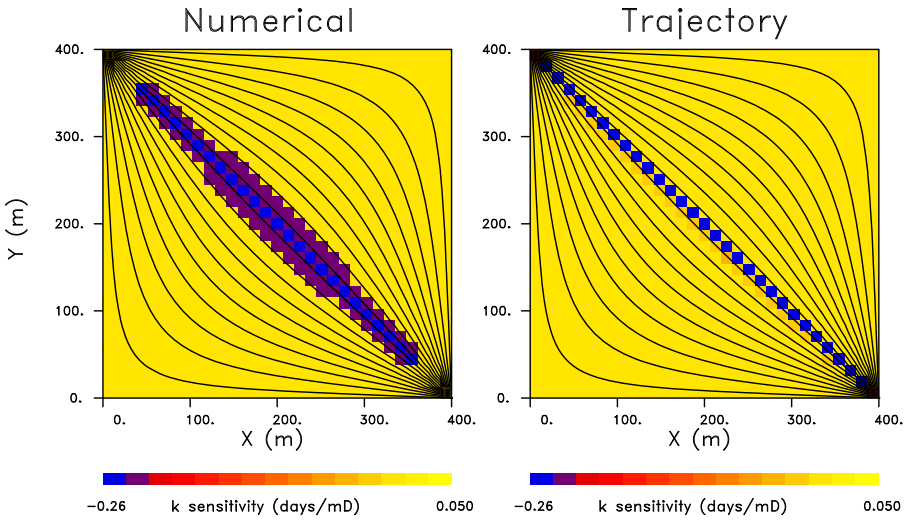

FIG. 14. (Left panel) Model parameter sensitivities computed using a numerical reservoir simulator and a perturbation approach. (Right panel) Model parameter sensitivities computed using the trajectory-based semi-analytical estimates given by Eq. (40).

simulations, where N is the number of grid blocks in the reservoir model. In this example, N equals 961, but it is typically much larger, in the hundreds of thousands to millions. There is overall agreement with the sensitivities, with peak sensitivities associated with the grid blocks that are close to the diagonal where the fastest propagation occurs.

IV. CONCLUSIONS

The work described here is just a first step in the development of trajectory-based modeling for multiphase flow. The primary objective of this study was to extend the approach, derived for the linear equations of quantum dynamics, to the case of two-phase flow, a process governed by non-linear partial differential equations. Thus, in the case of multiphase fluid flow, the saturation front velocity depends upon the saturation amplitude. In order to calculate the trajectories themselves, the simplest and most reliable procedure was adopted, based upon the output of a well-established numerical reservoir simulator TOUGH2. This methodology takes an easier off-the-shelf approach for calculating the paths, but if the work in quantum mechanical modeling is any indication, it is certainly not the most efficient computational technique.[14] The direct solution of the ordinary differential equations governing the trajectories should be far more efficient. For this reason, I have not conducted detailed comparisons of computer central processing unit (CPU) times for the extended trajectories with results from a purely numerical simulation. Such a comparison will be saved for a later study in which the direct trajectory calculations will be presented. A secondary objective of this work was an illustration of the trajectories and their changes in response to variations in the influence of gravity, and to variations in the relative permeability properties of the medium. The paths themselves were found to be very sensitive to the relative permeability properties of the medium, likely due to the non-linearity of the governing equations. The trajectories do indeed curve in response to the influence of gravitational forces, but that curvature appears to have a strong dependence on the two-phase properties of the medium.

The semi-analytical expressions that were derived offer some computational advantages in the calculation of sensitivities for the inverse problem, associated with imaging a medium using remotely gathered observations. In particular, a single numerical simulation of the complete set of component experiments is required in order to calculate all of the quantities needed for an update to a calculated image. The sensitivities follow from the semi-analytical expressions for the trajectories and the travel times and do not require the extensive computation of a perturbation approach nor the complexity of an adjoint formulation. The former methodology requires N + 1 complete numerical simulations in order to construct the needed sensitivities, where N is the number of parameters, which is typically of the order of the number of grid blocks in a reservoir simulation. The latter approach is based upon the development and solution of the adjoint problem, which can be complicated for applications involving multiphase fluid flow. The sensitivities derived here are approximate, but they are in general agreement with those provided by a numerical perturbation approach. An obvious application that needs to be explored is the use of the methodology for aquifer characterization and for the tomographic imaging of flow properties in the subsurface. Finally, this treatment of non-linear governing equations with spatially varying coefficients is also applicable to other models of fluid flow, such as multicomponent-multiphase flow, flow with coupled fluid momentum terms,[27,28] and the phase-field model described in the work of Cueto-Felgueroso and Juanes.[29]

ACKNOWLEDGMENTS

This work performed at Lawrence Berkeley National Laboratory was supported by the U.S. Department of Energy under Contract No. DE-AC02-05-CH11231 and Office of Basic Energy Sciences of the U.S. Department of Energy.

DATA AVAILABILITY

The data that support the findings of this study are available from the corresponding author upon reasonable request.

REFERENCES

[1] G. de Marsily, *Quantitative Hydrogeology* (Academic Press, San Diego, 1986).
[2] Y.-S. Wu, *Multiphase Flow in Porous and Fractured Reservoirs* (Elsevier, Amsterdam, 2016).
[3] D. Peaceman, *Fundamentals of Numerical Reservoir Simulation* (Elsevier, Amsterdam, 1977).
[4] A. Rabinovich, P. Bedrikovetsky, and D. M. Tartakovsky, "Analytical model for gravity segregation of horizontal multiphase flow in porous media," Phys. Fluids **32**, 046602-1–046602-15 (2020).
[5] S. J. Chapman, J. M. H. Lawry, and J. R. Ockendon, "Ray theory for high-Peclet-number convection diffusion," SIAM J. Appl. Math. **60**, 121–135 (1999).
[6] D. W. Vasco and A. Datta-Gupta, *Subsurface Fluid Flow and Imaging* (Cambridge University Press, Cambridge, 2016).
[7] D. Bohm, "A suggested interpretation of the quantum theory in terms of "hidden variables". I," Phys. Rev. **85**, 166–179 (1952).
[8] D. Bohm, "A suggested interpretation of the quantum theory in terms of "hidden variables". II," Phys. Rev. **85**, 180–193 (1952).
[9] E. R. Bittner, D. Kouri, S. Derrickson, and J. Maddox, "Variational quantum hydrodynamics," in *Applied Bohmian Dynamics: From Nanoscale Systems to Cosmology*, edited by X. Oriols and J. Mompart (Pan Stanford Publishing, Singapore, 2010).
[10] S. Garashchuk, "Quantum trajectory dynamics in imaginary time with the momentum-dependent quantum potential," J. Chem. Phys. **132**, 014112 (2010).
[11] S. Garashchuk and T. Vazhappilly, "Multidimensional quantum trajectory dynamics in imaginary time with approximate quantum potential," J. Phys. Chem. **114**, 20595–20602 (2010).
[12] S. Garashchuk, J. Mazzuca, and T. Vazhappilly, "Efficient quantum trajectory representation of wavefunctions evolving in imaginary time," J. Chem. Phys. **135**, 034104 (2011).
[13] Y. Goldfarb, I. Degani, and D. J. Tannor, "Bohmian mechanics with complex action: A new trajectory-based formulation for quantum mechanics," J. Chem. Phys. **125**, 231103-1–231103-4 (2006).
[14] R. E. Wyatt, *Quantum Dynamics with Trajectories* (Springer, New York, 2005).
[15] D. W. Vasco, S. R. Pride, C. Zahasky, and S. M. Benson, "Calculating trajectories associated with solute transport in a heterogeneous medium," Water Resour. Res. **54**, 6890–6908, https://doi.org/10.1029/2018WR023019 (2018).
[16] M. Th. van Genuchten, "A closed-form equation for predicting the hydraulic conductivity of unsaturated soils," Soil Sci. Soc. Am. J. **44**, 892–898 (1980).
[17] H. L. Stone, "Probability model for estimating three-phase relative permeability," J. Pet. Technol. **22**, 214–218 (1970).
[18] K. Pruess, C. Oldenburg, and G. Moridis, TOUGH2 User's Guide, Version 2.0, LBNL Report No. 43134, Berkeley, 1999.
[19] A. Datta-Gupta and M. J. King, *Streamline Simulation: Theory and Practice* (Society of Petroleum Engineers, Richardson, 2007).
[20] R. Courant and D. Hilbert, *Methods of Mathematical Physics* (John Wiley and Sons, New York, 1962).
[21] D. W. Vasco, "An extended trajectory mechanics approach for calculating the path of a pressure transient: Derivation and illustration," Water Resour. Res. **54**, 2642–2660, https://doi.org/10.1002/2017WR021360 (2018).
[22] J. R. Cash and A. H. Karp, "A variable order Runge-Kutta method for initial value problems with rapidly varying right-hand sides," ACM Trans. Math. Software **16**, 201–222 (1990).
[23] W. H. Press, S. A. Teukolsky, W. T. Vetterling, and B. P. Flannery, *Numerical Recipes* (Cambridge University Press, Cambridge, 1992).
[24] K. Li and R. N. Horne, "Comparison of methods to calculate relative permeability from capillary pressure in consolidated water-wet porous media," Water Resour. Res. **42**, 1–9, https://doi.org/10.1029/2005wr004482 (2006).
[25] J. C. Parker, R. J. Lenhard, and T. Kuppusamy, "A parametric model for constitutive properties governing multiphase flow in porous media," Water Resour. Res. **23**, 618–624, https://doi.org/10.1029/wr023i004p00618 (1987).
[26] D. W. Vasco and A. Datta-Gupta, "Asymptotics, saturation fronts, and high resolution reservoir characterization," Transp. Porous Media **42**, 315–350 (2001).
[27] P. Baveye and G. Sposito, "The operation significance of the continuum hypothesis in the water movement through soils and aquifers," Water Resour. Res. **20**, 521–530, https://doi.org/10.1029/wr020i005p00521 (1984).
[28] X. Pasquier, M. Quintard, and Y. Davit, "Modeling two-phase flow of immiscible fluids in porous media: Buckley-Leverett theory with explicit coupling terms," Phys. Rev. Fluids **2**, 104101-1–104101-19 (2017).
[29] L. Cueto-Felgueroso and R. Juanes, "A phase-field model of two-phase Hele-Shaw flow," J. Fluid Mech. **758**, 522–552 (2014).